Showcasing a cooperative research from Dr. Hung-Ju Yen's group, Institute of Chemistry, Academia Sinica and Professor Guey-Sheng Liou, Institute of Polymer Science and Engineering, National Taiwan University.

Redox-active polynaphthalimides as versatile electrode materials for high-voltage, high-rate and long-cycle-life organic Li-ion batteries

This work reports triphenylamine-based polynaphthalimides that can be fabricated as cathodes, anodes, and binders in lithium-ion batteries, simultaneously. The mechanistic studies revealed that the outstanding electrochemical performance of polynaphthalimide electrodes is highly related to the proper structural design thus fine-tuning their activation energy and charge-stored behavior as well as cycling stability. This work offers new opportunities for the development of various high-performance multifunctional energy storage systems for a wide range of applications.

As featured in:

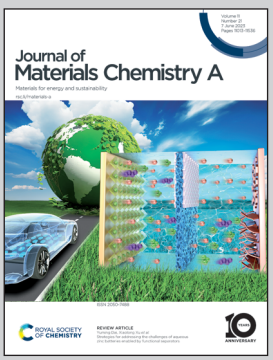

See Guey-Sheng Liou, Hung-Ju Yen *et al.*, *J. Mater. Chem. A*, 2023, **11**, 11210.

ROYAL SOCIETY OF CHEMISTRY

rsc.li/materials-a

Registered charity number: 207890

Journal of Materials Chemistry A

ROYAL SOCIETY OF CHEMISTRY

PAPER

View Article Online
View Journal | View Issue

Cite this: J. Mater. Chem. A, 2023, 11, 11210

Redox-active polynaphthalimides as versatile electrode materials for high-voltage, high-rate and long-cycle-life organic Li-ion batteries†

Febri Baskoro, [a] Andre Lammiduk Lubis, [a] Hui Qi Wong,[abc] Guey-Sheng Liou *[d] and Hung-Ju Yen *[a]

Multifunctional energy-storage devices show great promise in reducing the size and volume of devices, improving the storage capacity, and minimizing the cost of materials and fabrication while eliciting the benefits of additional functions to the system. Herein, we report three new triphenylamine-based polynaphthalimides (TPA-PNIs) that can work as a cathode, anode, and binder in lithium-ion batteries simultaneously. A TPA-PNI cathode delivered a high specific capacity up to 195 mA h g^{-1} after 100 cycles at 50 mA g^{-1}. A maximum capacity of 1092 mA h g^{-1} could be stored in the TPA-PNI anode after 100 cycles at 100 mA g^{-1}. A binder-free TPA-PNI cathode showed stable cycling performance with a maximum capacity of ~202 mA h g^{-1} after 100 cycles at 50 mA g^{-1}. TPA-PNI electrodes also demonstrated good cycling stability over 5000 cycles under a high current density of 2000 mA g^{-1}, as well as excellent rate capability at a current density up to 5000 mA g^{-1}. The electrochemical performance of TPA-PNI was among the best compared with that of other reported polymer-based electrodes. Detailed mechanistic studies and structural design of these ambipolar TPA-PNI electrodes could: (i) offer insights into the material selection and performance optimization of multifunctional energy storage devices at this early stage of research and development; and (ii) open new opportunities for the development of various high-performance multifunctional energy-storage systems for a wide range of applications.

Received 2nd February 2023
Accepted 11th April 2023

DOI: 10.1039/d3ta00596h

rsc.li/materials-a

Introduction

Thanks to light weight, high energy density, fast charging ability, and low self-discharge rate, lithium-ion batteries (LiBs) have crucial roles in portable energy-storage devices and have replaced many other energy-storage systems.[1–5] Besides their technological advancement, the use of inorganic electrode materials in LiBs is hindered by the limited source of non-earth-abundant elements, cost, and environmental unfriendliness.[6–9] Therefore, the utilization of sustainable and environmentally friendly materials is encouraged. Organic-based materials have been considered to be potential candidates for LiBs electrodes because they are cost-effective, sustainable, and can potentially deliver a high specific capacity with appropriate material/structural design.[10,11] Organic materials also offer flexibility in molecular structure for the design of a suitable electrode.[12] Organic materials such as organosulfur compounds,[13–17] organic radicals,[18–21] imine compounds,[22–24] azo compounds,[25–28] and carbonyl compounds[29–33] have been explored for employment as electrode materials for LiBs.

Carbonyl-based compounds have become potential candidates for organic-based electrodes due to their high theoretical capacity, abundant raw materials, and good electrochemical activity.[29,33,34] However, the use of carbonyl-based compounds is hindered due to their low electrical conductivity and high solubility in organic electrolytes.[12,35–37] Several approaches have been proposed to increase the solubility of organic-based compounds in an electrolyte solution: polymerization,[29,38,39] use of high-concentration electrolytes,[40,41] nanostructures,[42–44] and composite formation with advanced carbon materials.[25,45–47] Among those strategies, polymerization could solve the dissolution problem and improve the material stability of a carbonyl-based electrode in an electrolyte.[32,33,48,49]

[a]Institute of Chemistry, Academia Sinica, Taipei 115, Taiwan. E-mail: hjyen@gate.sinica.edu.tw

[b]Sustainable Chemical Science and Technology Program, Taiwan International Graduate Program (TIGP), Academia Sinica, National Taiwan University, Taipei 11529, Taiwan

[c]Department of Chemical Engineering, National Taiwan University, Taipei 10617, Taiwan

[d]Institute of Polymer Science and Engineering, National Taiwan University, Taipei 10617, Taiwan. E-mail: gsliou@ntu.edu.tw

† Electronic supplementary information (ESI) available: Supplementary notes, FTIR (Fig. S1 and S4), NMR spectra (Fig. S2, S3 and S5), TGA (Fig. S6), galvanostatic profile (Fig. S7, S14 and S16), Nyquist plots (Fig. S10 and S17), sweep rate analysis (Fig. S15), FESEM images (Fig. S11 and S12), *ex situ* XPS spectra (Fig. S8 and S13), GITT analysis (Fig. S9), supplementary tables (Tables S1–S5). See DOI: https://doi.org/10.1039/d3ta00596h

Polymerization could also open the opportunity of an active material having a dual role in the electrode (*i.e.*, simultaneous use of an active material and electrode binder), thereby reducing the production cost significantly.

As carbonyl-based compounds, polyimides (PIs) are high-performance polymeric materials due to their thermal stability, solvent resistance, good electrical and mechanical properties, and chemical resistance.[29,32,34] The redox-active carbonyl group in the structure of PIs is responsible for the Li-ion storage capability thanks to a two-electron enolization reaction as a cathode material.[29,33] Compared with small molecular imide analogs, PI cathode materials have improved cycling stability. However, they deliver a relatively lower specific capacity due to electrochemically inert units which are commonly used to link the electrochemically active imide moieties.[33,50] In addition, the low working potential of a PI cathode material based on an enolization reaction (2.0–2.5 V) hinders its practical application.[51] Therefore, an additional redox-active unit with higher voltage operation is needed to improve the electrochemical performance of a PI-based electrode.

Triphenylamine (TPA)-based polymers have been studied intensively due to their interesting physical properties: excellent charge transport, electroluminescence, as well as thermal and morphological stabilities.[52,53] In LiB applications, TPA has been reported to have high voltage operation and cycling stability if used as a cathode material.[53–55] The nitrogen radical in the TPA structure has been reported to participate actively in the electrochemical redox process, which can be reversibly doped and de-doped by PF_6^-.[51,53] However, the theoretical capacity of TPA is relatively low (109 mA h g^{-1}),[21,53] which is lower than the state-of-the-art $LiCoO_2$ (LCO; 140 mA h g^{-1}), which limits its practical application. TPA could be incorporated with a carbonyl-based compound to improve their electrochemical performance. Huang and colleagues reported a double-ion-embedded triphenylamine polymer (TPA-AQ) by introduction of an anthraquinone unit as a side-chain for a cathode LiB.[56] This polymeric design improved the battery performance by delivering an initial specific capacity of 159 and 106 mA h g^{-1} (after 100 cycles) at 0.1C and enhanced the working voltage up to 4.2 V. However, partial dissolution of the TPA-AQ polymer could be observed in the electrolyte after 24 h, which was responsible for the reduced cycling performance.[56] In addition, a crosslinked TPA-PI has been synthesized, resulting in a specific capacity of 125 mA h g^{-1} (at 0.1C) and relatively stable cycling up to 100 cycles.[57] Furthermore, a triphenylamine derivative, *N*,*N*,*N*′,*N*′-tetraphenyl-1,4-benzenediamine (TPPA), has been introduced in the PI structure *via* a one-step synthetic method, and improved the electrochemical performance of resulting hybrid polymer cathode significantly.[51] The reported TPPA–naphthalenediimide and TPPA–perylenediimide could deliver a specific capacity of 150.9 and 119.4 mA h g^{-1} after 70 cycles at 0.1C. However, this combination of TPPA and a PI unit as electrode material is still far from practical practical application in LiB.[29] Therefore, optimizing the molecular design of TPA-based PI cathode materials with good cycling stability, intrinsic high capacity, and excellent rate capability simultaneously is a challenge.

Herein, we report three new polynaphthalenediimides (PNIs) based on arylamine *via* one-step imidization for LiB electrodes: **PNI-1**, **PNI-2**, and **PNI-3** (Scheme 2). In this hybrid polymer design, the cyano functional group was introduced in the main backbone of the PNI-based polymer to lower the lowest unoccupied molecular orbital (LUMO) energy so that the reduction voltage and energy density could be boosted.[29] Results indicated that the TPA-PNIs polymer could serve as a cathode material, but could also be applied as an anode with excellent battery performance. A high specific capacity of 195 mA h g^{-1} after 100 cycles at a current density of 50 mA g^{-1} could be delivered by the TPA-PNI-based cathode. Meanwhile, as an anode, the TPA-PNIs-based material exhibited a maximum capacity of 1092 mA h g^{-1} after 100 cycles at 100 mA g^{-1}. The TPA-PNIs also demonstrated good cycling stability over 5000 cycles under a high current density as well as an excellent rate capability. Mechanistic studies revealed the outstanding electrochemical performance of TPA-PNIs materials to be closely related to an appropriate structural design based on tuning of activation energy and charge-stored behavior as well as cycling stability. Our study could unleash the full potential of PNIs for next-generation organic LiBs.

Results and discussion

Preparation and characterization of materials

A new diamine monomer, **Diamine-2**, was synthesized by hydrazine Pd/C-catalyzed reduction of the dinitro compound **1** resulting from the CsF-mediated aromatic nucleophilic substitution reaction of *N*,*N*′-di(4-nitrophenyl)-1,4-phenylenediamine with 4-fluorobenzonitrile (Scheme 1). Elemental analyses, Fourier transform-infrared (FT-IR) spectroscopy, and nuclear magnetic resonance (NMR) spectroscopy were used to identify the structures of the intermediate dinitro compound and targeted diamine monomer. The FT-IR spectra of both synthesized compounds are illustrated in Fig. S1.†

The nitro groups of compound **1** exhibited characteristic bands at 1584 and 1312 cm^{-1} due to NO_2 asymmetric and symmetric stretching, respectively, accompanied with a characteristic band for nitrile at 2220 cm^{-1} (C≡N stretching). After reduction to the diamine monomer, the characteristic absorption bands of the nitro group disappeared and the primary amino group showed a typical absorption pair at 3444 and 3359 cm^{-1} (N–H stretching). Fig. S2 and S3† illustrate the ^1H and ^{13}C NMR spectra of dinitro compound **1** and diamine

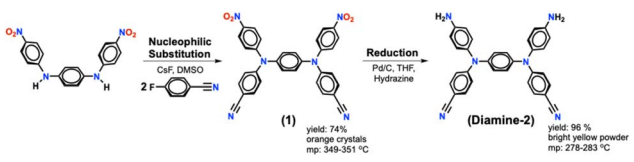

Scheme 1 Synthetic route to a TPPA-based diamine monomer: Diamine-2.

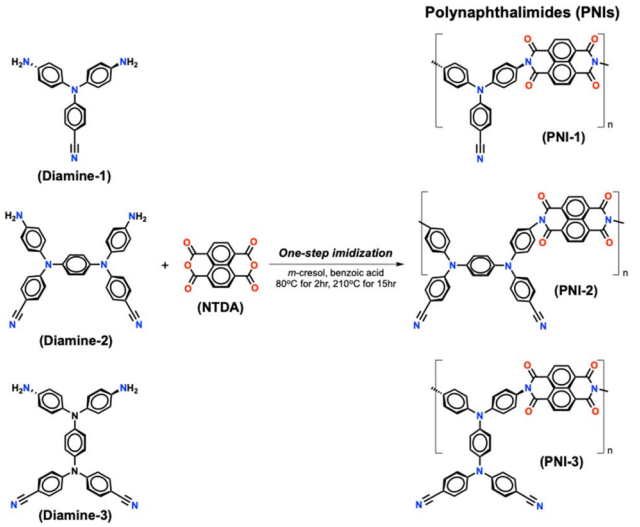

Scheme 2 Synthesis of polynaphthalimides by one-step polyimidization.

monomer **Diamine-2**, respectively, which agree well with the proposed molecular structures.

Three PNIs bearing pendent CN-TPA units were prepared by a one-pot, high-temperature solution polycondensation. Briefly, the dianhydride NTDA and diamines were polymerized in *m*-cresol at 210 °C in the presence of benzoic acid as the catalyst. Under these conditions, chain growth and imidization occurred spontaneously. The polymerization reactions proceeded homogenously and led to formation of highly viscous polymer solutions. The resulting polymer solutions precipitated into tough, fiber-like forms when poured slowly into methanol.

The inherent viscosities and solubility behavior of PNIs are summarized in Table S1,† and structural information was confirmed with IR and NMR spectroscopy. Fig. S4† shows the FT-IR spectra of as-synthesized PNIs, and reflects their structural similarity. The FT-IR spectra shown in Fig. S4† exhibited characteristic imide absorption bands at around 1715 (symmetrical C=O), 1675 (symmetrical C=O), 1345 (C–N), and 770 cm^{-1} (imide-ring deformation) with a characteristic band for nitrile at ~2222 cm^{-1} (C≡N stretching). Unlike the diamine monomers, PNIs are insoluble in most common organic solvents, which ultimately led to difficulties for full structural characterizations. The ^{1}H NMR spectra of PNIs in some conventional deuterated solvents such as $CDCl_3$ and dimethyl sulfoxide-d_6 (DMSO-d_6) showed no H signal due to their low solubility. Luckily, due to the strong protonation ability of concentrated sulfuric acid, **PNI-1** was found to exhibit limited solubility. Therefore, we could ascertain the exact structure of **PNI-1** *via* NMR spectra using D_2SO_4 as a solvent. As shown in Fig. S5,† five peaks were observed (corresponding to aromatic-*C*H carbons) in the distortionless enhancement by polarization transfer (DEPT)-135 spectrum for **PNI-1** and, along with ^{1}H NMR spectrum, the results suggested successful polyimidization and structural formation.

Thermogravimetric analysis (TGA) was employed to evaluate the thermal stability of the resulting PNIs. Fig. S6† shows the TGA curves of PNIs with a decomposition temperature (5% weight loss) >450 °C in nitrogen and air. Notably, the decomposition temperature of all PNIs was much higher than the working temperature of LiBs which, in general, lies between −20 °C and 80 °C. These data indicated that the PNIs satisfied the requirements of high thermal stability for LiBs.

Redox properties of TPA-PNI electrodes

Cyclic voltammetry (CV) was carried out by applying TPA-PNIs as LiB cathode and anode materials to ascertain the redox properties (Fig. 1). As the cathode, the CV of TPA-PNIs was undertaken in a potential window between 1.5 and 4.5 V (*vs.* Li/Li^+) at a scan rate of 0.1 mV s^{-1}; as the anode, it was operated within 0.02 and 3.0 V (*vs.* Li/Li^+). As shown in Fig. 1a, one reduction peak could be observed at 2.34 V in the cathodic scan of the **PNI-1** cathode, along with an oxidation peak at 2.47 V in

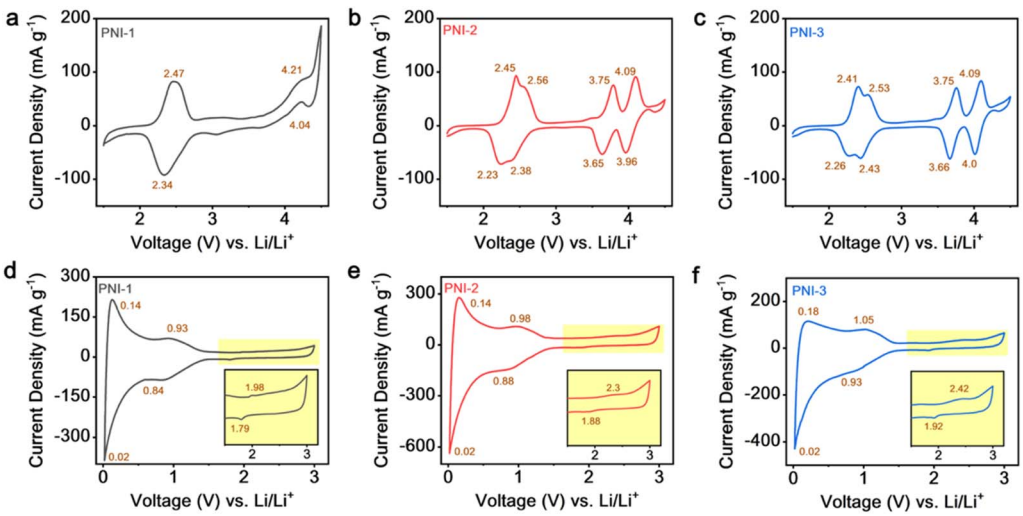

Fig. 1 Cyclic voltammetry of TPA-PNI electrodes as cathodes (a–c) and anodes (d–f) at a scan rate of 0.1 mV s^{-1}.

the anodic scan. This pair of redox peaks was associated with the two-electron enolization reaction of the naphthalenediimide (NTDI) unit.[29,32,51] Furthermore, the oxidation and reduction processes of the radical-cation triarylamine unit in **PNI-1** could be observed at 4.21 and 4.04 V, respectively, which suggested a successful doped/de-doped process of PF_6^-.[51,53,56] Interestingly, the well-defined two reduction peaks of the NTDI unit in **PNI-2** could also be observed in the cathodic scan but shifted slightly to a lower voltage at 2.23 and 2.38 V (difference of ~0.15 V), along with oxidation peaks at 2.45 and 2.56 V, than that of **PNI-1** (Fig. 1b). These phenomena could be ascribed to the presence of two cyano groups in **PNI-2**. The electron-withdrawing character of the cyano group has been reported to lower the LUMO energy of PIs and make them more reducible.[29,58] In addition, **PNI-3** (structural isomer of **PNI-2**) exhibited a slightly higher reduction potential of the NTDI unit at 2.26 and 2.43 V (with a higher potential difference of ~0.17 V) (Fig. 1c). This finding suggested that the different conformation of the cyano group in the polymer backbone had an important role in tuning the intrinsic properties of TPA-PNIs. At a higher operating voltage, **PNI-2** and **PNI-3** showed almost identical redox pairs at ~3.65/3.75 and 3.96/4.09 V (Fig. 1b and c), which could be ascribed to the doped/de-doped process of PF_6^- in the two radical nitrogen atom of diamine units.[51,53] The first redox couple at 3.65/3.75 V was attributed to the first reaction of the radical cation during p-type doping, and another redox couple at a higher potential (3.96/4.09 V) was associated with the reaction of the second radical cation.[53]

To further evaluate the TPA-PNI electrodes, we also elucidated their redox properties as an anode. As shown in Fig. 1d–f, all TPA-PNIs exhibited almost identical CV curves when applied as LiB anodes. As shown in Fig. 1d, reduction peaks were observed at a potential of 1.79, 0.84, and 0.02 V for **PNI-1**, accompanied with oxidation peaks at 1.98, 0.93, and 0.14 V, respectively. The first redox peak at 1.79/1.98 V could be attributed to the redox reaction of the carbonyl NTDI unit during the lithiation–de-lithiation process.[32,59] Meanwhile, the redox process at 0.84/0.93 V was ascribed to Li^+ insertion/de-insertion on the cyano group.[23] The Li^+ insertion/de-insertion on the carbonaceous units was noted at 0.02/0.14 V.[60,61] Although **PNI-2** and **PNI-3** had similar CV behavior to that of **PNI-1**, the redox potential associated with the NTDI unit was found at a slightly higher potential than that of **PNI-1** (Fig. 1e and f). This behavior could be related to the introduction of two cyano groups with a higher charge polarization and their electron-withdrawing character. Furthermore, the redox potential associated with NTDI unit in **PNI-3** was slightly higher than that of **PNI-2**. This finding again confirmed that the conformational unit position tuned the intrinsic electrochemical behavior of TPA-PNI-based electrodes.

Battery performance of TPA-PNI cathodes

To evaluate the battery performance of TPA-PNI cathodes, a half-cell LiB was assembled and charged–discharged galvanostatically at potential window of 1.5–4.5 V (*vs.* Li/Li^+). Fig. S7a–c† shows the galvanostatic charge–discharge profile of TPA-PNI cathodes at a current density of 50 mA g^{-1}. As depicted in Fig. S7a,† the **PNI-1** cathode exhibited a specific capacity of 125 mA h g^{-1} (after 100 cycles) along with a major plateau at 2.47 V. This plateau could be assigned to the enolization and dianion formation of the NTDI unit. Notably, the plateau ascribed to the doped/de-doped process of **PNI-1** was hardly

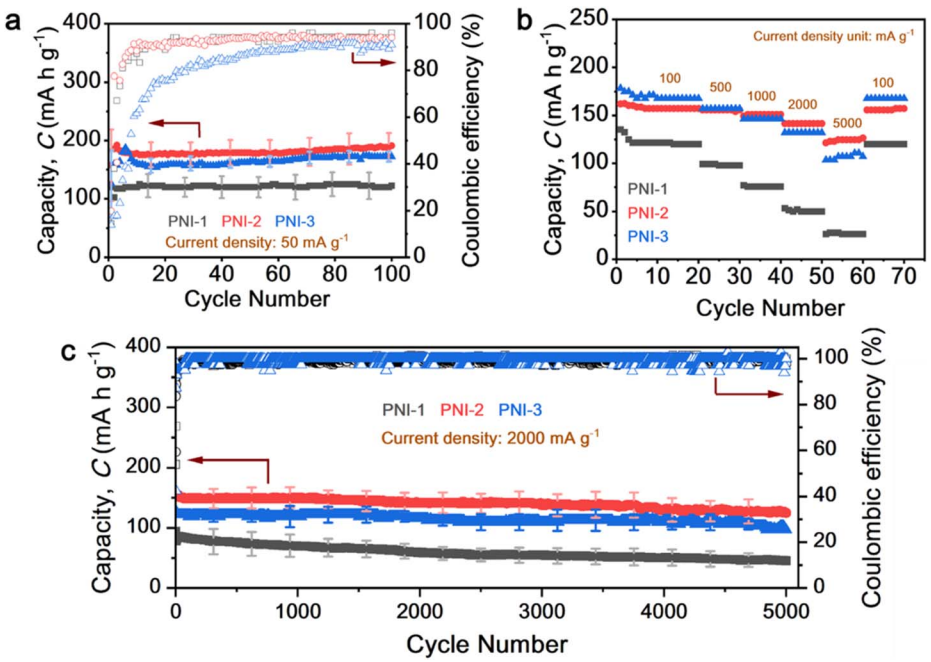

Fig. 2 Electrochemical performance of TPA-PNI cathodes. (a) Capacity profile at a current density of 50 mA g^{-1}. (b) Rate performance and (c) long cycling performance at 2000 mA g^{-1}.

seen in the galvanostatic profile. Furthermore, plateaus could be seen at 2.27, 3.67, and 3.98 V for **PNI-2** and **PNI-3**, respectively, indicating successful formation of the lithium enolate and dianion of the NTDI unit and doped/de-doped process of the nitrogen radical cation in the TPPA moiety. Interestingly, although **PNI-2** and **PNI-3** showed an almost identical galvanostatic profile, **PNI-2** had a significantly higher storage capacity (195 mA h g^{-1}) than that of **PNI-3** (170 mA h g^{-1}). This finding further indicated that the structural design played an important part in the performance of TPA-PNIs.

Fig. 2a shows the capacity profile of TPA-PNI cathodes at a current density of 50 mA g^{-1}. As shown in Fig. 2a, all TPA-PNI cathodes demonstrated stable cycling performance for up to 100 cycles. Notably, the **PNI-2** cathode exhibited the highest storage capacity of 195 mA h g^{-1}, with ~95% coulombic efficiency (CE), after 100 cycles at 50 mA g^{-1} than that of **PNI-1** (125 mA h g^{-1}) and **PNI-3** (170 mA h g^{-1}), indicating that an appropriate structural design boosted the performance of TPA-PNI cathode significantly. In addition, **PNI-2** and **PNI-3** showed a remarkable rate capability up to 5000 mA g^{-1} (Fig. 2b). **PNI-2** demonstrated a specific capacity of 162, 155, 151, 141, and 124 mA h g^{-1} at a current density of 100, 500, 1000, 2000, and 5000 mA g^{-1}, respectively. A specific capacity of 170, 153, 145, 134, and 112 mA h g^{-1} could be obtained by **PNI-3** at a current density of 100, 500, 1000, 2000, and 5000 mA g^{-1}, respectively. Unlike **PNI-2** and **PNI-3**, the **PNI-1** cathode exhibited a relatively low performance of rate capability. As depicted in Fig. 2b, the specific capacity of **PNI-1** was reduced significantly from 120, 98, 75, 47, and 26 mA h g^{-1} when the current density was 100, 500, 1000, 2000, and 5000 mA g^{-1}, respectively. Even so, the long-cycling performance indicated that all TPA-PNI cathodes demonstrated excellent stability and reversibility by retaining their high capacity up to 130 mA h g^{-1} over 5000 cycles under a high current density of 2000 mA g^{-1} (Fig. 2c). This outstanding performance of TPA-PNI cathodes was outperformed among the reported organic polymeric battery cathodes (Table S4†).

To investigate the storage mechanism in TPA-PNI cathodes, *ex situ* X-ray photoelectron spectroscopy (XPS) was carried out for **PNI-2** at different stages (Fig. S8†). As shown in Fig. S8a,† the C 1s spectra of the fresh **PNI-2** cathode (before cycling) and full discharge stage were found similar by exhibiting four peaks which could be ascribed to the binding energy (BE) of C–C, C–N, C=O, and π–π at 284.5, 285.7, 288.6, and 290.7 eV, respectively. However, these spectra were different than that at the fully charged stage. A new BE of C–O could be observed at 286.2 eV during full charging, indicating successful association of Li^+ on the carbonyl group in the NTDI unit. Furthermore, a new BE of PF_6^- at 685.5 eV was observed in F 1s spectra at the fully charged stage (Fig. S8b†). This peak then disappeared at the discharge stage, indicating successful doping/de-doping of PF_6^-. In good agreement with F 1s spectra, the N 1s spectra of **PNI-2** slightly shifted from 400.4 eV to 399.6 eV at the fully charged stage and recovered back during full discharge (Fig. S8c†). This process could be ascribed to the reduction of electron density of the N atom on the TPPA unit during oxidation of the radical.[20]

Based on the *ex situ* XPS study, Scheme 3 was proposed to represent the possible reaction of TPA-PNI cathodes during the electrochemical process. The enolization reaction of NTDI units took place at 1.5–3.0 V (Fig. 1a–c). In this voltage range, two electron-transfer processes facilitated the carbonyl group in the NTDI unit to mobilize their electrons and form delocalized carbonyl sites, which was accompanied by the association and dissociation of Li^+.[29,32] Furthermore, the doped/de-doped process of the nitrogen radical cation in TPPA units took place at a higher potential window (3.3–4.3 V). As depicted in Scheme 3a, PF_6^- could be reversibly inserted into the TPA unit within **PNI-1** at a potential of 3.9–4.3 V, which was identified by

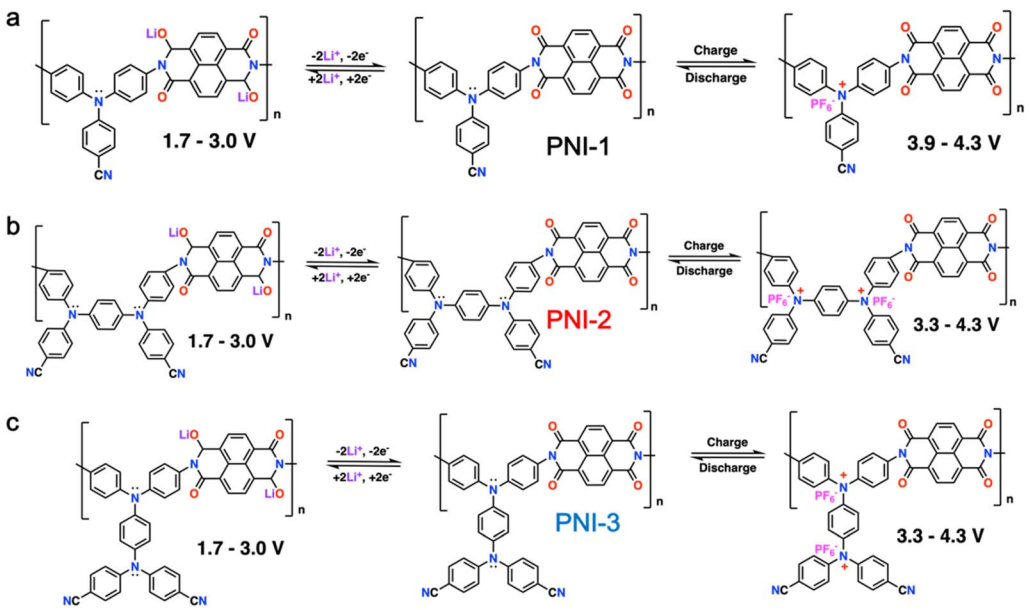

Scheme 3 Reaction mechanism of TPA-PNI cathodes (schematic).

a small redox peak at 4.21 and 4.04 V (Fig. 1a). Meanwhile, two PF_6^- anions could be stored in the TPPA units of **PNI-2** and **PNI-3** *via* two-electron transfer (Scheme 3b and c). This process was depicted by symmetrical redox peaks at around 3.65/3.75 and 4.0/4.10 V (Fig. 1b and c).

To further investigate ion diffusion in PNI systems, the galvanostatic intermittent titration technique (GITT) was carried out at 50 mA g^{-1}. As shown in Fig. S9,† the diffusion coefficient for Li^+ (D_{Li^+}) was found at around 10^{-9} to 10^{-10} cm^2 s^{-1} at a potential of ~2.5–4.3 V during charge–discharge. Interestingly, **PNI-2** had a slightly faster D_{Li^+} at a potential of 3.5–4.2 V than that of **PNI-3**. This finding indicated that the structural design in **PNI-2** could promote higher charge mobilization. In addition, electrochemical impedance spectroscopy (EIS) was carried out to probe the interfacial resistance and transport properties in TPA-PNI cathodes before and after cycling. Fig. S10† shows the Nyquist plots of TPA-PNI cathodes before and after 200 cycles at 100 mA g^{-1}. As shown in Fig. S10,† one semicircle was observed for all TPA-PNI cathodes in the mid-frequency region, along with typical Warburg impedance in the low-frequency region. This semicircle could be ascribed to charge transfer resistance (R_{ct}) in the electrode interphase (Fig. S10d†). Interestingly, all TPA-PNIs demonstrated significant reduction in semicircles after 200 cycles (Fig. S10a–c†). As presented in Table S2,† the R_{ct} of TPA-PNIs was reduced from 375.90, 336.50, and 276.60 Ω (before cycling) to 191.80, 88.29, and 105.64 Ω (after 200 cycles) for **PNI-1**, **PNI-2**, and **PNI-3**, respectively. These data indicated a faster charge-transport ability of TPA-PNI cathodes due to the formation of a less resistive interphase during cycling. Importantly, **PNI-2** had the lowest R_{ct} after 200 cycles than that of **PNI-1** and **PNI-3** (Table S2†), suggesting that appropriate arrangement of structural/conformational units had important roles in the charge-transfer ability of TPA-PNI cathodes, and could improve the storage capacity (Fig. 2). Moreover, in good agreement with R_{ct} values, the D_{Li^+} of **PNI-2** after cycling was one order magnitude faster (1.96×10^{-12} cm^2 s^{-1}) than that of **PNI-3** (6.96×10^{-13} cm^2 s^{-1}), and two orders of magnitude faster than **PNI-1** (6.19×10^{-14} cm^2 s^{-1}) (Table S2†). These data further confirmed that the structural design in **PNI-2** could provide significantly better Li^+ mobility during cycling, which was responsible for its outstanding storage capability.

Series of spectroscopy analysis were carried out at different cycling intervals to probe the stability of PNIs under long-term operation. Surface and cross-sectional field emission scanning electron microscopy (FESEM) images were obtained to evaluate morphological changes. As shown in Fig. S12,† the morphology of electrodes was changed significantly after 5000 cycles compared with that before cycling (Fig. S11†). As depicted in Fig. S12,† significantly reduced porosity can be observed on surface and cross-sectional images of PNI cathodes after 5000 cycles, which possibly resulted from electrolyte decomposition. Notably, although the electrode morphology was changed, there were no significant changes for PNI-active materials after 5000 cycles. This observation confirmed their excellent material stability during long cycling operations. In addition, *ex situ* XPS was also used for **PNI-2** as a representative of PNI cathodes under long-term operation. As depicted in Fig. S13,† the specific BE of C–C, C–N, and C=O remained at 284.75, 285.90, and 288.70 eV, respectively, on C 1s spectra after 5000 cycles (Fig. S13a†). The BE of C≡N, N-amine, and N-imide was observed at 399.05, 400.01, and 400.80 eV, respectively, on N 1s spectra (Fig. S13b†) before and after 5000 cycles. These data further confirmed the excellent stability of PNIs under long cycling operations.

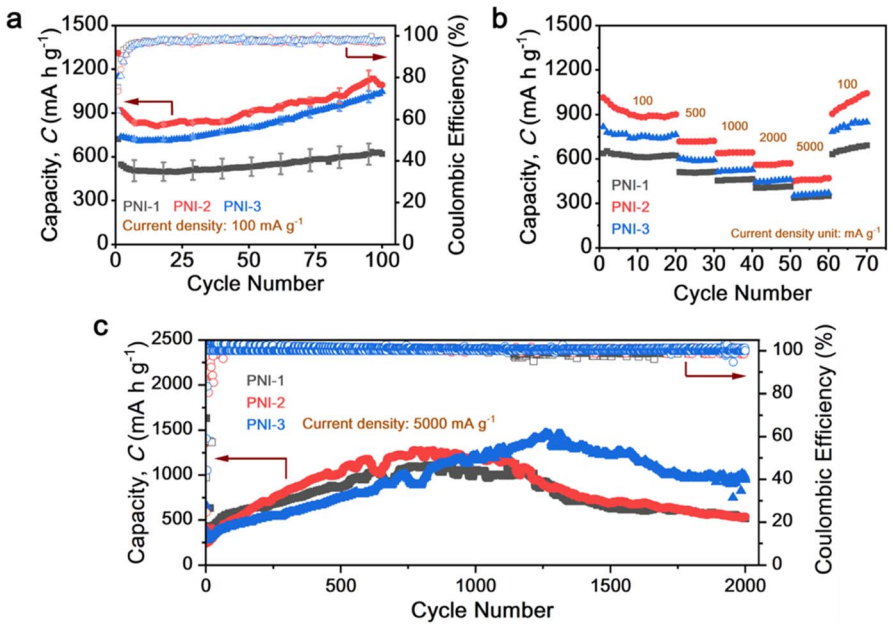

Fig. 3 Electrochemical performance of TPA-PNIs as anodes. (a) Capacity profile at a current density of 100 mA g^{-1}. (b) Rate performance and (c) long cycling performance at 5000 mA g^{-1}.

Battery performance of TPA-PNI anodes

To probe the capability of TPA-PNIs as LiB anodes, half-cell LiBs were fabricated and charged–discharged galvanostatically at a potential window of 0.02–3.0 V (*vs.* Li/Li^+). As depicted in Fig. S14,† two major plateaus could be seen for all TPA-PNI anodes at ~0.9 and ~0.02 V, along with slightly increased capacity during cycling at 100 mA g^{-1}. These similar plateaus in the galvanostatic profile indicated an identical Li^+-storage characteristic for all TPA-PNI anodes, which was in good agreement with CV data (Fig. 1d–f). Moreover, the **PNI-1** anode exhibited a specific discharge capacity of 520 mA h g^{-1} during an initial five cycles, before it gradually increased up to 650 mA h g^{-1} after 100 cycles. **PNI-2** and **PNI-3** anodes also demonstrated a gradual increase in capacity up to 1100 mA h g^{-1} after 100 cyclic. In line with the galvanostatic profile, the increasing specific capacity is clearly depicted in Fig. 3a. The overall increased capacity during cycling could be associated by two parameters. First, it could be assigned to the increasing Li^+ transport during cycling. Second, it was related to the activation period for TPA-PNIs to get Li-binding sites fully lithiated.[12,32,35,62–65] The phenomenon of increasing capacity has also been reported for other polymeric anodes.[23,60] Notably, the electrochemical performance of TPA-PNI anodes is among the best as compared with reported polymeric battery anodes (Table S5†).

Furthermore, the TPA-PNI anodes showed excellent rate capability up to 5000 mA g^{-1} (Fig. 3b). As shown in Fig. 3b, a reversible capacity of 611, 508, 460, 408, and 344 mA h g^{-1} was obtained for the **PNI-1** anode when the current density varied from 100, 500, 1000, 2000 to 5000 mA g^{-1}, respectively. In good agreement with the capacity profile, **PNI-2** delivered the highest specific capacity of 920, 756, 632, 582, and 450 mA h g^{-1} at a current density of 100, 500, 1000, 2000, and 5000 mA g^{-1}, respectively. **PNI-3** exhibited a specific capacity of ~760, 605, 490, 410, and 350 mA h g^{-1} at a current density of 100, 500, 1000, 2000, and 5000 mA g^{-1}, respectively. This outstanding rate capability was confirmed by the recoverable specific capacity of 650, 1130, and 970 mA h g^{-1} for **PNI-1**, **PNI-2**, and **PNI-3**, respectively, when the current density was switched back to 100 mA g^{-1} (Fig. 3b). Moreover, this long cycling performance indicated that TPA-PNI anodes could sustain up to 2000 cycles under a significantly high current density of 5000 mA g^{-1} (Fig. 3c). As shown in Fig. 3c, a peak capacity of 1000, 1350, and 1375 mA h g^{-1} was observed for **PNI-1** (after 625 cycles), **PNI-2** (after 680 cycles), and **PNI-3** (after 1250 cycles), respectively.

Scheme S1† represents the possible reaction mechanism of TPA-PNI anodes during charge–discharge. It has been reported that four carbonyl groups in naphthalimide units can be fully utilized to accommodate Li^+ binding sites *via* a four-electron transfer reaction as LiB anodes,[32,61,66,67] and so are additionally responsible for the storage capability of four Li-ions. Unlike graphitic carbon, which limits its storage capacity of 372 mA h g^{-1} *via* formation of LiC_6, each carbonaceous benzene ring in a polymer structure has been reported to be capable of reversibly storing up to six Li-ions and form Li_6C_6 species.[68] Therefore, TPA-PNI anodes could reversibly store up to 37, 50, and 50 Li^+ for **PNI-1**, **PNI-2**, and **PNI-3**, respectively (Scheme S1†).

As illustrated in Scheme S1,† two reaction steps were assumed to take place during charge–discharge. First, four Li^+ were attached to four carbonyl groups in the NTDI unit during the first reduction. This process was followed by further Li^+ insertion in the cyano groups and aromatic rings of TPA-PNI anodes to form Li_6C_6, which was consistent with the three reduction peaks on CV curves. Furthermore, Faraday's law can be applied to estimate the theoretical capacity of TPA-PNI anodes using the following equation: $C\ (\text{mA h g}^{-1}) = \dfrac{n \times F}{3.6M}\ (\text{mA h g}^{-1})$, where C represents the theoretical capacity of TPA-PNI, n is the total number of electrons received, F is the Faraday constant (96 485 C mol^{-1}), and M is the molecular mass of the repeating unit.[32,69,70] Hence, the

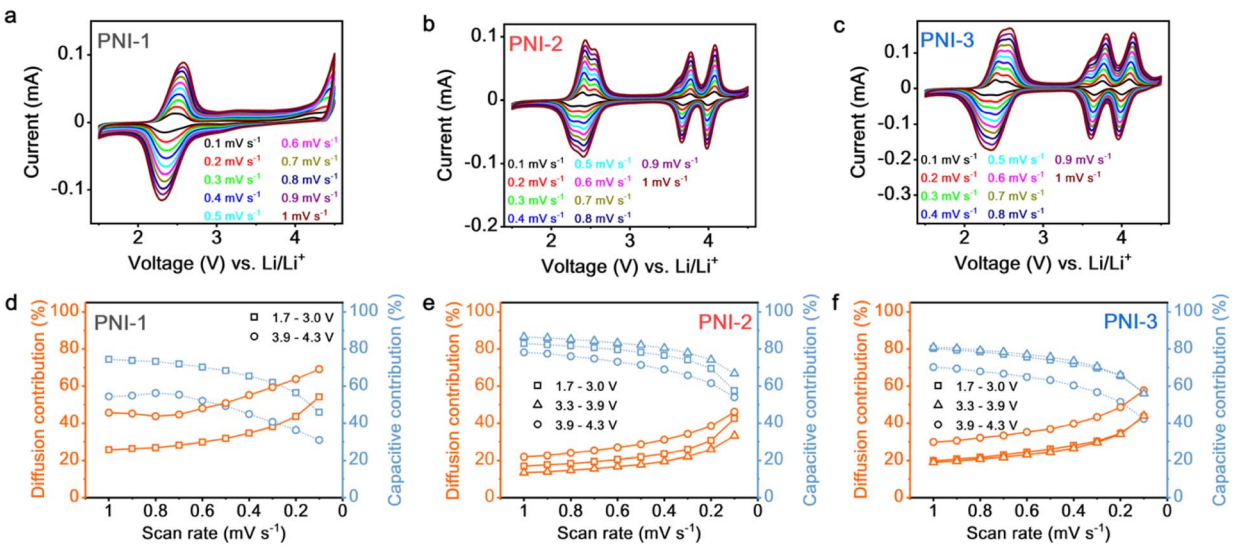

Fig. 4 Sweep rate CV and charge-storage contribution at different voltage ranges. (a and d) **PNI-1**; (b and e) **PNI-2**; (c and f) **PNI-3**.

theoretical capacity of **PNI-1**, **PNI-2**, and **PNI-3** was estimated to be 1762, 1775, and 1775 mA h g^{-1}, respectively.

Mechanistic studies of TPA-PNI electrodes

To gain deeper understanding of the charge-storage behavior for diamine and the NTDI units in TPA-PNI electrodes, we undertook sweep rate CV at scan rates of 0.1–1.0 mV s^{-1} (ESI Text 3†). Fig. 4a, d and h show the typical CV curves of **PNI-1**, **PNI-2**, and **PNI-3** cathodes, respectively, at various scan rates. They depict a gradual increase in the total current as the scan rate varied from 0.1 to 1.0 mV s^{-1}. Further analysis of the total current at different voltage ranges revealed the *b*-value of TPA/TPPA and NTDI units in TPA-PNIs to be 0.61–0.89 (Fig. S15a–c†), indicating that the total charge stored in TPPA and the NTDI unit resulted from the synergetic contribution of diffusion and a surface-controlled (capacitive) process. The quantitative analysis of capacitive ($k_1\nu$) and diffusion ($k_2\nu^{1/2}$) contributions in the TPPA and NTDI units of TPA-PNI cathodes could be obtained from the slope and intercept from the $i/\nu^{1/2}$ against $\nu^{1/2}$ plot, respectively (Fig. S15d–f†). As shown in Fig. 4d, the NTDI unit (voltage range, 1.7–3.0 V) in **PNI-1** exhibited nearly 70% capacitive contribution at a high scan rate of 1–0.5 mV s^{-1}, before gradually decreasing up to 46% at 0.1 mV s^{-1}. A similar trend could be observed at the TPA unit (voltage range, 4.0–4.3 V) in **PNI-1**, which showed a gradual decrease in capacitive contribution from ~50% at a high scan rate of 1–0.5 mV s^{-1} to 34% at a scan rate of 0.1 mV s^{-1}.

Interestingly, replacing a diamine unit from TPA to TPPA tuned the charge-storage characteristics of TPA-PNIs significantly. As depicted in Fig. 4e and f, attaching a TPPA unit to the PNIs **PNI-2** and **PNI-3** drastically increased the capacitive contribution in the total charge stored of the NTDI unit by nearly 80% at a high scan rate of 1–0.5 mV s^{-1} and 40% at the lowest scan rate of 0.1 mV s^{-1}. Furthermore, the two radicals of nitrogen in TPPA exhibited almost similar behavior by delivering nearly 80% capacitive contribution at scan rate of 1–0.5 mV s^{-1} that decreased gradually to ~55% at 0.1 mV s^{-1} (Fig. 4e and f). This phenomenon could have resulted from the –C≡N functional group having an almost identical electronic environment as that of TPPA. As shown in Fig. 4f, the diffusion contribution in the NTDI unit from **PNI-3** was increased nearly by 3% than that of **PNI-2**. The increase in diffusion contribution could also be observed for the TPPA unit (Fig. 4e). The diffusion contribution for the first radical cation in **PNI-3**, which was close to the nitrogen atom with two –C≡N functional groups (at a potential of 3.3–3.9 V), was found to exhibit ~5% more diffusion contribution at a high scan rate of 1–0.5 mV s^{-1} and an almost 10% increase at the lowest scan rate of 0.1 mV s^{-1} (Fig. 4f) than that of **PNI-2** (Fig. 4e). Meanwhile, the second radical cationin **PNI-3** at a potential of 3.9–4.3 V (close to naphthalimide linkage) had an even higher diffusion contribution of 8% at a scan rate of 1–0.5 mV s^{-1} and 12% at 0.1 mV s^{-1} (Fig. 4f) than that of **PNI-2** (Fig. 4e). These data again confirmed that a different conformational position in the polymer backbone had an important role in tuning charge-storage behavior.

Next, EIS was employed to further evaluate the activation energy (E_a). It has been reported that the relationship between the exchange current (i_0) and charge transfer resistance at the electrode interface (R_{ct}) at various temperatures could be used to estimate the E_a using the Arrhenius equation: $i_0 = RT/nFR_{ct}$ and $i_0 = A\exp(-E_a/RT)$, where A is a temperature-independent coefficient, R is the gas constant, T (K) is the absolute temperature, n is the number of transferred electrons, F is the Faraday constant, and E_a is the apparent activation energy.[71,72] As shown in Fig. 5a–c, all TPA-PNIs exhibited one semicircle which decreased gradually as the temperature increased, which clearly indicated a decreasing R_{ct}. Furthermore, the E_a of TPA-PNIs could be estimated from: $E_a = -Rk\ln 10$, k is the slope of the fitting line of the Arrhenius plots (log10 i_0 as a function of 1000/T) (Fig. 5d). Then, the E_a of TPA-PNIs was estimated to be 14.35, 33.98, and 41.79 kJ mol^{-1} for **PNI-1**, **PNI-2**, and **PNI-3**, respectively. Interestingly, the lowest E_a resulted from **PNI-1**, which indicated that the structure with a TPA unit required the minimum energy to promote a charge-transfer reaction than the other PNIs. Notably, **PNI-3** was found to have a higher E_a (41.79 kJ mol^{-1}) than that of **PNI-2** (33.98 kJ mol^{-1}), indicating that more energy was required to activate its charge-transfer reaction. The higher E_a required for **PNI-3** could have resulted from a higher charge polarization in the molecular structure, which was consistent with the capacity profile showing **PNI-3** to have a slightly lower capacity than that of **PNI-2** as the cathode and anode. In summary, we found that different molecular structures and conformations had crucial roles in tuning the charge-storage behavior and E_a of TPA-PNIs, which further impacted their electrochemical performance as materials for LiB electrodes.

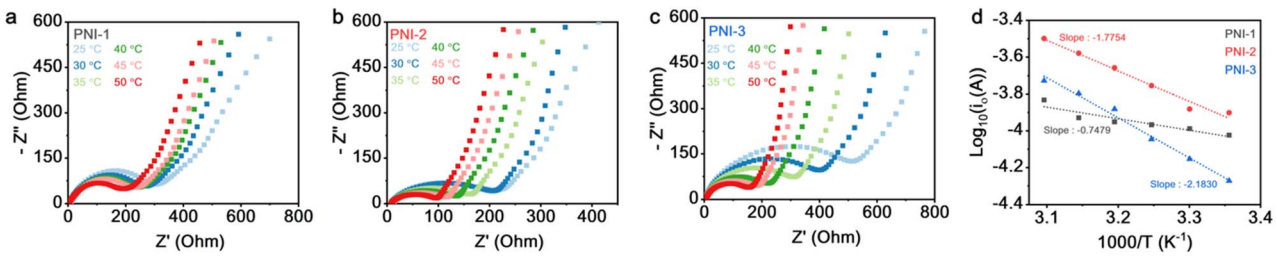

Fig. 5 Calculation of the activation energy of TPA-PNIs. Nyquist plot of (a) **PNI-1**, (b) **PNI-2**, and (c) **PNI-3** at various temperatures, respectively. (d) Log i_0 *vs.* 1000/T plot.

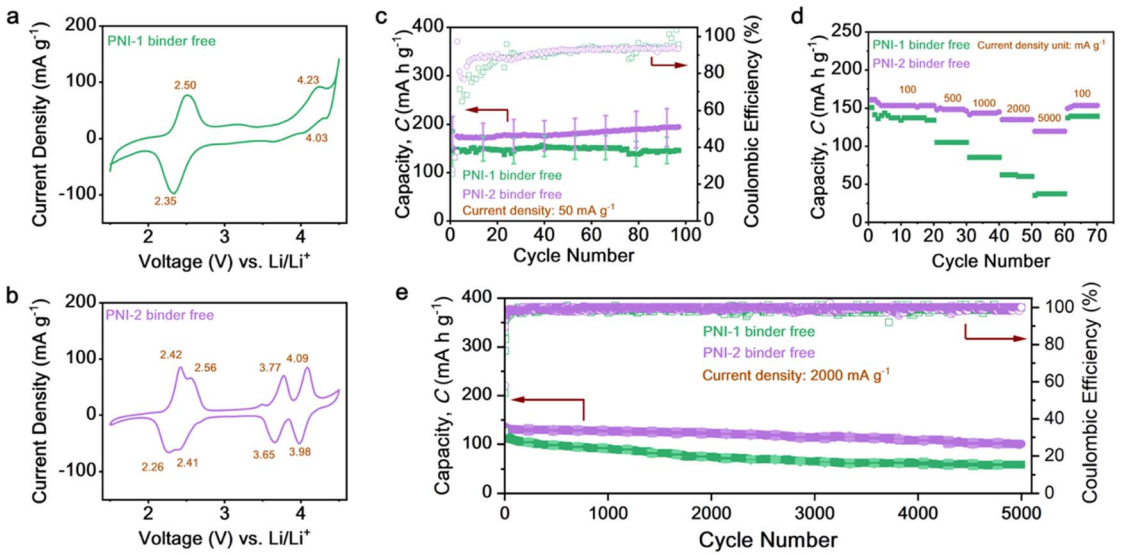

Fig. 6 Electrochemical performance of binder-free TPA-PNI cathodes. CV of (a) binder-free **PNI-1** and (b) binder-free **PNI-2**, respectively. (c) Capacity profile at 50 mA g^{-1}. (d) Rate performance and (e) long cycling performance at 2000 mA g^{-1}.

Battery performance of binder-free PNI electrodes

To further investigate the multifunctional capability of TPA-PNIs as cathode/anode materials and electrode binders simultaneously, we undertook a battery test with a binder-free cathode (weight ratio of active material : conductive carbon = 40 : 60) for **PNI-1** and **PNI-2**. As shown in Fig. 6a and b, a significant change was not observed in the CV curve of binder-free electrodes from electrodes containing a PVDF binder, thereby indicating a well-preserved redox capability. The binder-free **PNI-1** (Fig. 6a) exhibited a reduction peak at 2.35 V, along with its oxidation at 2.50 V, which corresponded to enolization on the NTDI unit. A PF_6^- doped/de-doped process on TPA was observed at 4.23/4.03 V. Furthermore, **PNI-2** demonstrated a well-preserved redox capability by exhibiting its pair redox potential for enolization on NTDI and doped/de-doped TPPA (Fig. 6b). In addition, the galvanostatic profile of binder-free cathodes (Fig. S16†) showed good agreement with their CV results. As shown in Fig. S16a,† plateaus at 2.47 and 2.34 V were observed for binder-free **PNI-1**, which could be assigned to enolization of the NTDI unit. However, the plateau associated with the doped/de-doped process originating from TPA could not be observed clearly in the galvanostatic profile. In addition, the binder-free **PNI-2** exhibited plateaus at 2.27, 2.41, 3.67, and 3.98 V, indicating successful formation of lithium enolate and dianions of the NTDI unit, as well as the doped/de-doped process of TPPA.

Furthermore, the cycling performance of binder-free **PNI-1** and **PNI-2** (Fig. 6c) at 50 mA g^{-1} exhibited a comparable specific capacity with that of binder (Fig. 2a). As shown in Fig. 6c, the binder-free **PNI-1** and **PNI-2** cathodes showed a stable cycling performance for up to 100 cycles with a capacity of 160 and 202 mA h g^{-1} at 50 mA g^{-1}. This specific capacity was even higher than for their respective electrodes with a PVDF binder (Fig. 2a). EIS was applied to understand the transport properties in binder-free cathodes. As shown in Fig. S17,† a significant reduction on the semicircle was observed on binder-free **PNI-1** and binder-free **PNI-2** after cycling. This decreased semicircle was associated with a significantly reduced R_{ct} of binder-free cathodes, from 222.03 to 119 Ω for **PNI-1** and 313.96 to 57.64 Ω for **PNI-2**, respectively, indicating a better transport ability after cycling (Table S3†). Notably, the higher D_{Li^+} of binder-free cathodes than that with the PVDF binder might have resulted from the formation of a homogeneous slurry (even without a PVDF binder) and a higher conductive content of a binder-free cathode (60% Super P) than that with a binder (50% Super P), which improved the transport property and storage capability significantly.

Besides the superior capacity, binder-free **PNI-1** and binder-free **PNI-2** cathodes also exhibited an excellent rate capability at a current density of up to 5000 mA g^{-1} (Fig. 6d). This excellent rate performance was confirmed by the highest storage capacity of 137 mA h g^{-1} (binder-free **PNI-1**) and 152 mA h g^{-1} (binder-free **PNI-2**) being recovered if the current density was turned back to 100 mA g^{-1}. Furthermore, binder-free **PNI-1** and binder-free **PNI-2** cathodes showed exceptional long cycling stability up to 5000 cycles under a high current density of 2000 mA h g^{-1} (Fig. 6e). As shown in Fig. 6e, the long cycling capability was confirmed by maintaining capacity retention >45% and 75% for binder-free **PNI-1** and binder-free **PNI-2**, respectively. The electrochemical performance further suggested that TPA-PNIs could serve as multifunctional components in LiBs as active materials and a binder simultaneously.

Conclusions

We demonstrated an efficient storage capability of newly designed (TPA-PNIs) that could work as cathodes and anodes for LiBs simultaneously. By taking advantage of the high capacity and low solubility of naphthalimide, the hybrid TPA-

PNIs exhibited outstanding electrochemical performance and operation durability. The TPA-PNI cathode could deliver a high specific capacity up to 195 mA h g^{-1} at 50 mA g^{-1} after 100 cycles. A maximum capacity of 1092 mA h g^{-1} could be stored in the TPA-PNI anode after 100 cycles at 100 mA g^{-1}. A binder-free TPA-PNI cathode could deliver a stable cycling performance with a maximum capacity of ~202 mA h g^{-1} at 50 mA g^{-1} after 100 cycles. TPA-PNI electrodes also demonstrated good cycling stability over 5000 cycles under a high current density of 2000 mA g^{-1}, as well as an excellent rate capability up to 5000 mA g^{-1}. Mechanistic studies revealed that the outstanding electrochemical performance of TPA-PNIs was closely related with an appropriate structural design to fine-tune their E_a, charge-stored behavior, and cycling stability.

Experimental section

Materials

4,4′-Diamino-4″-cyanotriphenylamine (**Diamine-1**),[73] *N*,*N*-bis(4-aminophenyl)-*N*′,*N*′-di(4-cyanophenyl)-1,4-phenylenediamine (**Diamine-3**)[74] and *N*,*N*′-di(4-nitrophenyl)-1,4-phenylenediamine[75] were synthesized according to a previously reported procedure. Commercially available aromatic tetracarboxylic dianhydride 1,4,5,8-naphthalenetetracarboxylic dianhydride (NTDA) (TCI) was purified by vacuum sublimation. Carbon black, conductive carbon (Super P®; >99% (metal basis)), polyvinylidene fluoride (PVDF; Alfa Aesar), and *N*-methylpyrrolidone (NMP; >99%; Thermo Fisher Scientific) were procured. Lithium hexafluorophosphate ($LiPF_6$; 1 M) in ethylene carbonate (EC) and diethyl carbonate (DEC) (1 : 1 v/v) were purchased from UBIQ Technology. All materials were used as received without further purification.

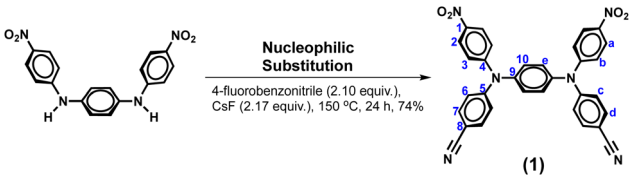

***N*,*N*′-Bis(4-nitrophenyl)-*N*,*N*′-di(4-cyanophenyl)-1,4-phenylenediamine (1).** To a solution of 7.32 g (20.88 mmol) of *N*,*N*′-di(4-nitrophenyl)-1,4-phenylenediamine and 5.37 g (43.87 mmol) of 4-fluorobenzonitrile in 70 mL of dried dimethyl sulfoxide (DMSO), 6.96 g (45.37 mol) of dried cesium fluoride was added with stirring, and the mixture was heated at 150 °C for 24 h under a nitrogen atmosphere. The mixture was poured into methanol/water, and the precipitated red powder was collected by filtration and reprecipitated by *N*,*N*-dimethylformamide/methanol. The product was filtered to afford 8.58 g (74% yield) of orange crystals with a melting point of 349–351 °C. FT-IR (KBr): 1312, 1584 cm^{-1} (NO_2 stretch), 2223 cm^{-1} (C≡N stretch). ^{1}H NMR (500 MHz, DMSO-d_6, δ, ppm): 7.19 (d, J = 9.2 Hz, 4H), 7.29 (s, 4H), 7.31 (d, J = 8.8 Hz, 4H), 7.83 (d, J = 8.8 Hz, 4H), 8.18 (d, J = 9.2 Hz, 4H). ^{13}C NMR (125 MHz, DMSO-d_6, δ, ppm): 105.87, 118.59 (–C≡N), 121.51, 124.18, 125.50, 128.45, 133.94, 141.52, 142.33, 149.34, 151.70. Anal. calcd (%) for $C_{32}H_{20}N_6O_4$ (552.54): C, 69.56; H, 3.65; N, 15.21. Found: C, 69.32; H, 4.19; N, 15.15.

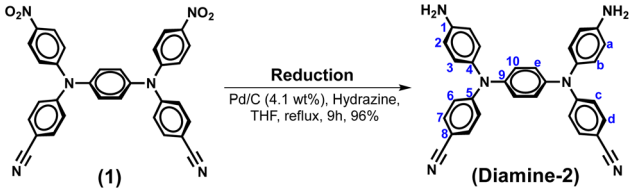

***N*,*N*′-Bis(4-aminophenyl)-*N*,*N*′-di(4-cyanophenyl)-1,4-phenylenediamine (Diamine-2).** In a 250 mL three-neck round-bottomed flask equipped with a stirring bar under a nitrogen atmosphere, 9.78 g (17.71 mmol) of dinitro compound **1** and 0.40 g of 10% Pd/C were dissolved/suspended in 100 mL of tetrahydrofuran. The suspension was heated to reflux, and 5.0 mL of hydrazine monohydrate was added slowly to the mixture. After the solution had been stirred at a reflux temperature for 9 h, the solution was filtered to remove Pd/C, and the filtrate was cooled. The product was collected by filtration and dried *in vacuo* at 80 °C to give 8.34 g (96% yield) of bright-yellow powder with a melting point of 278–283 °C. FT-IR (KBr): 3359, 3444 cm^{-1} (N–H stretch), 2220 cm^{-1} (C≡N stretch). ^{1}H NMR (500 MHz, DMSO-d_6, δ, ppm): 5.26 (s, 4H, $-NH_2$), 6.62 (d, J = 8.6 Hz, 4H), 6.74 (d, J = 9.0 Hz, 4H), 6.92 (d, J = 8.6 Hz, 4H), 7.18 (s, 4H), 7.52 (d, J = 9.0 Hz, 4H). ^{13}C NMR (125 MHz, DMSO-d_6, δ, ppm): 99.04, 114.96, 116.31, 119.77 (–C≡N), 126.70, 128.61, 132.72, 133.15, 141.93, 147.55, 151.90. Anal. calcd (%) for $C_{32}H_{24}N_6$ (492.57): C, 78.03; H, 4.91; N, 17.06. Found: C, 77.71; H, 5.34; N, 17.12.

Preparation of polynaphthalimides (PNIs) by a one-step method. Three naphthenic polyimides (polynaphthalimides; PNIs) were synthesized from diamine monomers and dianhydride NTDA. The synthesis of **PNI-2** was used as an example to illustrate the general synthetic route. To a solution of 753.8 mg (1.54 mmol) of **Diamine-2** in 7.0 mL of *m*-cresol, 410.4 mg (1.54 mmol) of NTDA was added in one portion, then 752.5 mg of benzoic acid was added. The mixture was heated at 80 °C for 2 h, and then at 210 °C for 15 h. The obtained polymer solution was poured slowly into 300 mL of stirred methanol, giving rise to a brown fibrous precipitate that was collected by filtration, washed thoroughly with methanol, and dried under a vacuum at 100 °C. Re-precipitations of the polymer by NMP/methanol were carried out twice for further purification. The inherent viscosity of **PNI-2** was 0.45 dL g^{-1} in *m*-cresol at a concentration of 0.5 g dL^{-1} at 30 °C.

Material characterization

Fourier transform infrared (FTIR) spectroscopy was done on a 6600 system (JASCO). Elemental analyses were run in an elemental analyzer (VarioEL-III CHNS; Heraeus). NMR spectroscopy was undertaken on a FT-NMR spectrometer (AVANCE-500; Bruker) using tetramethylsilane as an internal reference, and peak multiplicity was reported as singlet and doublet. The inherent viscosity was determined at a concentration of 0.5 g dL^{-1} using a viscometer (TV-2000; Tamson) at 30 °C. TGA was conducted using a Pyris 1 system (PerkinElmer). Experiments

were carried out on approximately 6–8 mg film samples heated in flowing nitrogen or air (flow rate = 20 cm^3 min^{-1}) at a heating rate of 20 °C min^{-1}. CV was carried out using an electrochemical analyzer (MultiPalmSens4; PalmSens). EIS was conducted before and after cycling using an electrochemical workstation (model 760e; CH Instruments). Cells were charged and discharged galvanostatically using a battery station system (AcuTech Systems). The GITT was undertaken using a potentiostat (Squidstat; Admiral Instruments).

Author contributions

F. B. and A. L. L. contributed equally. G. S. L. and H. J. Y. designed the experiments. F. B. and A. L. L. carried out the electrochemical and characterization experiments. H. Q. W. undertook characterizations. The manuscript was written and edited by F. B. and H. J. Y. All authors discussed the results and reviewed the manuscript.

Conflicts of interest

There are no conflicts to declare.

Acknowledgements

F. Baskoro acknowledges the postdoctoral fellowship program supported by Academia Sinica (AS-PD-11201-M04). H.-J. Yen acknowledges the financial support by Innovative Materials and Analysis Technology Exploration in Academia Sinica (AS-iMATE-111-21) and the Ministry of Science and Technology in Taiwan (MOST 111-2124-M-001-001; MOST 108-2113-M-001-023-MY3; NSTC 111-2113-M-001-051).

Notes and references

1 L. Long, S. Wang, M. Xiao and Y. Meng, *J. Mater. Chem. A*, 2016, **4**, 10038–10069.
2 B. Dunn, H. Kamath and J.-M. Tarascon, *Science*, 2011, **334**, 928.
3 J. M. Tarascon and M. Armand, *Nature*, 2001, **414**, 359.
4 P. G. Bruce, B. Scrosati and J.-M. Tarascon, *Angew. Chem., Int. Ed.*, 2008, **47**, 2930–2946.
5 J. B. Goodenough and Y. Kim, *Chem. Mater.*, 2010, **22**, 587–603.
6 P. Rohland, E. Schröter, O. Nolte, G. R. Newkome, M. D. Hager and U. S. Schubert, *Prog. Polym. Sci.*, 2022, **125**, 101474.
7 K. Liu, Y. Liu, D. Lin, A. Pei and Y. Cui, *Sci. Adv.*, 2018, **4**, eaas9820.
8 C. Liu, Z. G. Neale and G. Cao, *Mater. Today*, 2016, **19**, 109–123.
9 A. Manthiram, *Nat. Commun.*, 2020, **11**, 1550.
10 D. Larcher and J. M. Tarascon, *Nat. Chem.*, 2015, **7**, 19–29.
11 P. Poizot and F. Dolhem, *Energy Environ. Sci.*, 2011, **4**, 2003–2019.
12 S. Lee, G. Kwon, K. Ku, K. Yoon, S.-K. Jung, H.-D. Lim and K. Kang, *Adv. Mater.*, 2018, **30**, 1704682.
13 A. Wild, M. Strumpf, B. Häupler, M. D. Hager and U. S. Schubert, *Adv. Energy Mater.*, 2017, **7**, 1601415.
14 X. Zhang, K. Chen, Z. Sun, G. Hu, R. Xiao, H.-M. Cheng and F. Li, *Energy Environ. Sci.*, 2020, **13**, 1076–1095.
15 D.-Y. Wang, Y. Si, W. Guo and Y. Fu, *Nat. Commun.*, 2021, **12**, 3220.
16 D.-Y. Wang, W. Guo and Y. Fu, *Acc. Chem. Res.*, 2019, **52**, 2290–2300.
17 D.-Y. Wang, Y. Si, J. Li and Y. Fu, *J. Mater. Chem. A*, 2019, **7**, 7423–7429.
18 T. Sukegawa, A. Kai, K. Oyaizu and H. Nishide, *Macromolecules*, 2013, **46**, 1361–1367.
19 C. Friebe and U. S. Schubert, *Top. Curr. Chem.*, 2017, **375**, 19.
20 Y. Ou, Y. Xiong, Z. Hu, Y. Zhang and L. Dong, *J. Mater. Chem. A*, 2022, **10**, 10373–10382.
21 C. Su, H. He, L. Xu, K. Zhao, C. Zheng and C. Zhang, *J. Mater. Chem. A*, 2017, **5**, 2701–2709.
22 T. Matsunaga, T. Kubota, T. Sugimoto and M. Satoh, *Chem. Lett.*, 2011, **40**, 750–752.
23 Z. Man, P. Li, D. Zhou, R. Zang, S. Wang, P. Li, S. Liu, X. Li, Y. Wu, X. Liang and G. Wang, *J. Mater. Chem. A*, 2019, **7**, 2368–2375.
24 K. Sakaushi, E. Hosono, G. Nickerl, T. Gemming, H. Zhou, S. Kaskel and J. Eckert, *Nat. Commun.*, 2013, **4**, 1485.
25 C. Peng, G.-H. Ning, J. Su, G. Zhong, W. Tang, B. Tian, C. Su, D. Yu, L. Zu, J. Yang, M.-F. Ng, Y.-S. Hu, Y. Yang, M. Armand and K. P. Loh, *Nat. Energy*, 2017, **2**, 17074.
26 G. Zhao, Y. Zhang, Z. Gao, H. Li, S. Liu, S. Cai, X. Yang, H. Guo and X. Sun, *ACS Energy Lett.*, 2020, **5**, 1022–1031.
27 C. Luo, X. Ji, S. Hou, N. Eidson, X. Fan, Y. Liang, T. Deng, J. Jiang and C. Wang, *Adv. Mater.*, 2018, **30**, 1706498.
28 C. Luo, O. Borodin, X. Ji, S. Hou, K. J. Gaskell, X. Fan, J. Chen, T. Deng, R. Wang, J. Jiang and C. Wang, *Proc. Natl. Acad. Sci. U. S. A.*, 2018, **115**, 2004–2009.
29 Z. Song, H. Zhan and Y. Zhou, *Angew. Chem., Int. Ed.*, 2010, **49**, 8444–8448.
30 P. Sharma, D. Damien, K. Nagarajan, M. M. Shaijumon and M. Hariharan, *J. Phys. Chem. Lett.*, 2013, **4**, 3192–3197.
31 L. Mu, Y. Lu, X. Wu, Y. Ding, Y.-S. Hu, H. Li, L. Chen and X. Huang, *Green Energy Environ.*, 2018, **3**, 63–70.
32 K. B. Labasan, H.-J. Lin, F. Baskoro, J. J. H. Togonon, H. Q. Wong, C.-W. Chang, S. D. Arco and H.-J. Yen, *ACS Appl. Mater. Interfaces*, 2021, **13**, 17467–17477.
33 J. Wang, H. Liu, C. Du, X. Zhang, Y. Liu, H. Yao, Z. Sun and S. Guan, *Chem. Eng. J.*, 2022, **444**, 136598.
34 H. Wang, C.-J. Yao, H.-J. Nie, K.-Z. Wang, Y.-W. Zhong, P. Chen, S. Mei and Q. Zhang, *J. Mater. Chem. A*, 2020, **8**, 11906–11922.
35 Y. Lu, Q. Zhang, L. Li, Z. Niu and J. Chen, *Chem*, 2018, **4**, 2786–2813.
36 H. Oubaha, J.-F. Gohy and S. Melinte, *ChemPlusChem*, 2019, **84**, 1179–1214.
37 H. Lyu, X.-G. Sun and S. Dai, *Adv. Energy Sustainability Res.*, 2021, **2**, 2000044.
38 T. Nokami, T. Matsuo, Y. Inatomi, N. Hojo, T. Tsukagoshi, H. Yoshizawa, A. Shimizu, H. Kuramoto, K. Komae,

H. Tsuyama and J.-i. Yoshida, *J. Am. Chem. Soc.*, 2012, **134**, 19694–19700.
39 S. Muench, A. Wild, C. Friebe, B. Häupler, T. Janoschka and U. S. Schubert, *Chem. Rev.*, 2016, **116**, 9438–9484.
40 J. Yang, Z. Wang, Y. Shi, P. Sun and Y. Xu, *ACS Appl. Mater. Interfaces*, 2020, **12**, 7179–7185.
41 T. Cai, Y. Han, Q. Lan, F. Wang, J. Chu, H. Zhan and Z. Song, *Energy Storage Mater.*, 2020, **31**, 318–327.
42 F. Wan, X.-L. Wu, J.-Z. Guo, J.-Y. Li, J.-P. Zhang, L. Niu and R.-S. Wang, *Nano Energy*, 2015, **13**, 450–457.
43 Y. Wang, Y. Ding, L. Pan, Y. Shi, Z. Yue, Y. Shi and G. Yu, *Nano Lett.*, 2016, **16**, 3329–3334.
44 M. Lee, J. Hong, J. Lopez, Y. Sun, D. Feng, K. Lim, W. C. Chueh, M. F. Toney, Y. Cui and Z. Bao, *Nat. Energy*, 2017, **2**, 861–868.
45 W. Guo, Y.-X. Yin, S. Xin, Y.-G. Guo and L.-J. Wan, *Energy Environ. Sci.*, 2012, **5**, 5221–5225.
46 Z. Song, T. Xu, M. L. Gordin, Y.-B. Jiang, I.-T. Bae, Q. Xiao, H. Zhan, J. Liu and D. Wang, *Nano Lett.*, 2012, **12**, 2205–2211.
47 C. Luo, Y. Zhu, Y. Xu, Y. Liu, T. Gao, J. Wang and C. Wang, *J. Power Sources*, 2014, **250**, 372–378.
48 X. Han, C. Chang, L. Yuan, T. Sun and J. Sun, *Adv. Mater.*, 2007, **19**, 1616–1621.
49 J. Kim, J. H. Kim and K. Ariga, *Joule*, 2017, **1**, 739–768.
50 Q. Zhang, G. Lin, Y. He, X. Cui and Y. Yang, *Mater. Today Chem.*, 2020, **17**, 100341.
51 C. Zhang, S. Chen, G. Zhou, Q. Hou, S. Luo, Y. Wang and G. Shi, *J. Electrochem. Soc.*, 2021, **168**, 050548.
52 H.-J. Yen and G.-S. Liou, *Polym. Chem.*, 2018, **9**, 3001–3018.
53 C. Su, F. Yang, L. Ji, L. Xu and C. Zhang, *J. Mater. Chem. A*, 2014, **2**, 20083–20088.
54 J. K. Feng, Y. L. Cao, X. P. Ai and H. X. Yang, *J. Power Sources*, 2008, **177**, 199–204.
55 C. Zhang, X. Yang, W. Ren, Y. Wang, F. Su and J.-X. Jiang, *J. Power Sources*, 2016, **317**, 49–56.
56 W. Huang, T. Jia, G. Zhou, S. Chen, Q. Hou, Y. Wang, S. Luo, G. Shi and B. Xu, *Electrochim. Acta*, 2018, **283**, 1284–1290.
57 S. Chen, T. Jia, G. Zhou, C. Zhang, Q. Hou, Y. Wang, S. Luo, G. Shi and Y. Zeng, *J. Electrochem. Soc.*, 2019, **166**, A2543–A2548.
58 S. Chopin, F. Chaignon, E. Blart and F. Odobel, *J. Mater. Chem.*, 2007, **17**, 4139–4146.
59 J. Wang, H. Yao, C. Du and S. Guan, *J. Power Sources*, 2021, **482**, 228931.
60 H. Kang, H. Liu, C. Li, L. Sun, C. Zhang, H. Gao, J. Yin, B. Yang, Y. You, K.-C. Jiang, H. Long and S. Xin, *ACS Appl. Mater. Interfaces*, 2018, **10**, 37023–37030.
61 J. Wu, X. Rui, C. Wang, W.-B. Pei, R. Lau, Q. Yan and Q. Zhang, *Adv. Energy Mater.*, 2015, **5**, 1402189.
62 S. Renault, V. A. Oltean, C. M. Araujo, A. Grigoriev, K. Edström and D. Brandell, *Chem. Mater.*, 2016, **28**, 1920–1926.
63 H. Yang, S. Liu, L. Cao, S. Jiang and H. Hou, *J. Mater. Chem. A*, 2018, **6**, 21216–21224.
64 B. T. McAllister, E. Grignon, T. B. Schon, S. Y. An, C.-H. Yim, Y. Abu-Lebdeh and D. S. Seferos, *ACS Appl. Energy Mater.*, 2021, **4**, 6659–6666.
65 Z. Zhang, Y. Zhou, P. Chen, S. Zeng, W. Nie and Y. Xu, *ACS Appl. Energy Mater.*, 2021, **4**, 12882–12891.
66 J. He, Y. Liao, Q. Hu, Z. Zeng, L. Yi, Y. Wang, H. Lu and M. Pan, *J. Power Sources*, 2020, **451**, 227792.
67 Z. Ba, Z. Wang, Y. Zhou, H. Li, J. Dong, Q. Zhang and X. Zhao, *ACS Appl. Energy Mater.*, 2021, **4**, 13161–13171.
68 X. Han, G. Qing, J. Sun and T. Sun, *Angew. Chem., Int. Ed.*, 2012, **51**, 5147–5151.
69 J. Li, M. Luo, Z. Ba, Z. Wang, L. Chen, Y. Li, M. Li, H.-B. Li, J. Dong, X. Zhao and Q. Zhang, *J. Mater. Chem. A*, 2019, **7**, 19112–19119.
70 F. Baskoro, C.-M. Ngue, K. B. Labasan, H. Q. Wong, M.-K. Leung and H.-J. Yen, *Energy Technol.*, 2021, **9**, 2100212.
71 Y. Yamada, Y. Iriyama, T. Abe and Z. Ogumi, *J. Electrochem. Soc.*, 2010, **157**, A26.
72 J. Xu, I.-Y. Jeon, J.-M. Seo, S. Dou, L. Dai and J.-B. Baek, *Adv. Mater.*, 2014, **26**, 7317–7323.
73 L. Li, R. Kikuchi, M.-A. Kakimoto, M. Jikei and A. Takahashi, *High Perform. Polym.*, 2005, **17**, 135–147.
74 G. S. Liou, C. W. Chang, H. J. Yen, J. P. Pan, C. R. Yang, T. H. Wang, J. M. Hsu (Industrial Technology Research Institute; ITRI), *US Pat.*, US8088932B2, 2012.
75 I. Różalska, P. Kułyk and I. Kulszewicz-Bajer, *New J. Chem.*, 2004, **28**, 1235–1243.